A Study on Er^{3+} Substitution in Sol-gel $BaTiO_3$ Thin Films Using X-ray Line Profile Analysis

Zeen Vee OOI, Ala'eddin A. SAIF *

School of Microelectronic Engineering, University Malaysia Perlis, Pauh Putra Campus, 02600 Arau, Perlis, Malaysia

crossref http://dx.doi.org/10.5755/j01.ms.23.3.16225

Received 10 September 2016; accepted 01 December 2016

Perovskite erbium doped barium titanate ($Ba_{1-x}Er_xTiO_3$) thin films, at different *x* values, have been fabricated on SiO_2/Si substrate and characterized using X-ray diffraction (XRD) in the range of 20° to 60° to study the phase structure and geometric parameters for the films. XRD patterns show a broadening and shifting for the perovksite peaks toward higher angle due to Er^{3+} doping. The effect of Er^{3+} substitution into $BaTiO_3$ lattice has been deeply investigated using X-ray line profine analysis through Scherrer equation, Williamson-Hall and size-strain plot (SSP) approaches. For all approaches used, it has been found that the crystallite size for the films decreases as the value of *x* increases, which is attributed to the relatively small Er^{3+} ionic size compared to Ba^{2+}. In Williamson-Hall and SSP analysis, it is found that the microstrain created due to Er^{3+} doping causes distortion for the lattice and broadening for perovskite peaks as a result. Among all approaches used in this work, SSP shows to be the most suitable for this type of materials by giving the best fitted plots and goodness of fit R^2 close to 1.

Keywords: $Ba_{1-x}Er_xTiO_3$, sol-gel, X-ray line profile analysis, crystallite size, microstrain.

1. INTRODUCTION

In recent years, lead-free ferroelectric Erbium doped Barium Titanate (Er:$BaTiO_3$) has received considerable attention as a candidate for microelectronic and optoelectronic devices due to the desirable properties, such as excellent dielectric, ferroelectric, and enhanced electro-optic properties [1]. This material can be synthesized in thin film form using various techniques, such as sol-gel deposition, RF sputtering, and metal organic chemical vapour deposition (MOCVD) [1 – 3]. However, phase structure of materials is an essential step to be understood prior studying the electrical and optical characteristics, since the material's properties directly affected by its structure. The crystalline structure is usually identified via X-ray diffraction (XRD), which is also reported to be capable to uncover the crystallite size of the scanned material [4 – 5].

Recently, it is found that crystallite size is one of the keys that influence the ferroelectric properties of ferroelectric thin films including the Curie point, polarization, switching speed, etc. [6]. In theoretical prediction, if the crystallite size is less than certain critical value, the ferroelectric effect will be diminished and the paraelectric state takes place [6]. Furthermore, it is essential to have a precise approximation of crystallite size for materials with crystallite size of order of less than 100 nm [4]. Among the crystallite size measurement approaches, X-ray diffraction considered the simplest and easiest to estimate the crystallite size for materials. In which the X-ray line profile analysis (XLPA) principle, includes Scherrer equation, Williamson-Hall analysis, and size-strain plot (SSP) method, is used to determine the crystallite size based on peak broadening [5, 7].

Several works have been reported the crystallite size analysis on the pure and doped $BaTiO_3$ nanoparticles [8 – 10]. However, such detailed analysis have not yet been applied to Er:$BaTiO_3$ thin films. In this work, $Ba_{1-x}Er_xTiO_3$ thin films are fabricated on SiO_2/Si substrate using sol-gel technique. In order to obtain the crystalline structure for the films, they are annealed at 700 °C. The prepared samples are scanned using XRD to determine the crystalline structure and phase information. Finally, the geometric parameters, such as crystallite size, lattice strain, and stress are investigated via X-ray line profile analysis.

2. EXPERIMENTAL DETAILS

2.1. Solution preparation

Three different solutions, i.e. $BaTiO_3$, $Ba_{0.9}Er_{0.1}TiO_3$, and $Ba_{0.8}Er_{0.2}TiO_3$ solutions were prepared using barium acetate, erbium acetate, and titanium (IV) isopropoxide as starting materials. Acetic acid and 2-methoxyethanol were employed to dissolve acetates and titanium (IV) isopropoxide, respectively. A specific amount of acetates were added into a pre-heated acetic acid to form Ba-Er solution. This solution was then refluxed at 120 °C for 2 hours. Another solution was prepared by adding stoichiometric amount of titanium (IV) isopropoxide into 2-methoxyethanol under stirring. Finally, both solutions were mixed at room temperature and refluxed at 120 °C for 1 hour.

2.2. Sample preparation and characterization

$Ba_{1-x}Er_xTiO_3$ thin films were fabricated on SiO_2/Si substrate using spin-coating method. The substrates were initially cleaned with acetone, isopropyl alcohol, and

* Corresponding author. Tel.: +60-14-2470306.
E-mail address: *alaeddinsaif@gmail.com* (Ala'eddin A. Saif)

deionized water. The solutions were deposited on the prepared substrates using spin-coater at 5000 rpm for 20 s, and then baked at 200 °C. The spin-coating and baking processes were repeated until desired thickness was obtained. The final thin films were then annealed at 700 °C for 1 hour.

X-ray diffraction (XRD) was utilized to reveal the crystallinity information of the $Ba_{1-x}Er_xTiO_3$ thin films within the range of 20° to 60°. A 1.54 Å X-ray was radiated from copper target, with the operating voltage of 40 kV and operating current of 30 mA.

3. RESULTS AND DISCUSSION

3.1. Phase analysis

Fig. 1 illustrates the XRD patterns for undoped and Er-doped $BaTiO_3$ samples. The XRD graphs are matched with JCPDS entry 05-0626, which shows that $Ba_{1-x}Er_xTiO_3$ films are crystallized with perovskite structure and the perovskite peaks are indexed accordingly. There are no secondary phases observed within these films, indicating that no byproducts or interdiffusion is occurred with the substrate, leading to a good film quality. However, a small peak is noticed at $2\theta \approx 32.96°$ for certain samples, corresponding to the silicon substrate and it has no relation with perovskite $Ba_{1-x}Er_xTiO_3$ films. According to Zaumseil [11], this silicon peak can produce zero intensity for certain plane orientation of the sample, ϕ, thus, could produce non-similar behaviour in all samples.

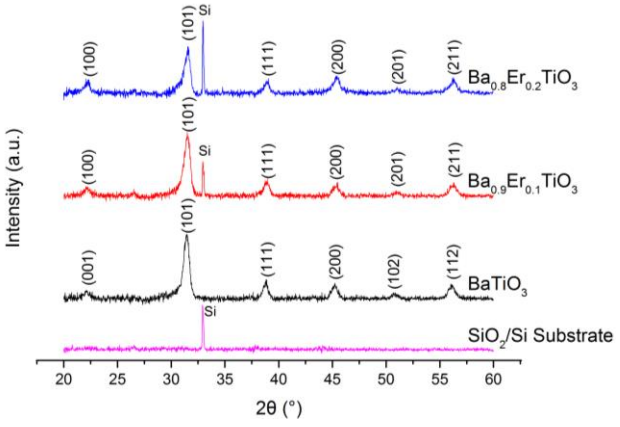

Fig. 1. X-ray diffraction patterns of $Ba_{1-x}Er_xTiO_3$ thin films

From Fig. 1, it can be noticed that as $BaTiO_3$ film is doped with Er^{3+} ions and their concentration increases, the perovskite peaks are shifted toward higher angle. This shifting could be due to the lattice deformation as a result of Er^{3+} ions substitution. However, it is interesting to mention here that the shifting of some peaks, particularly at $2\theta = 21.10647°$, 50.778°, and 56.05863°, causes the lattice to be oriented with different miller indices for the Er-doped $BaTiO_3$ samples as indicated in the figure, which is also attributed to the lattice distortion.

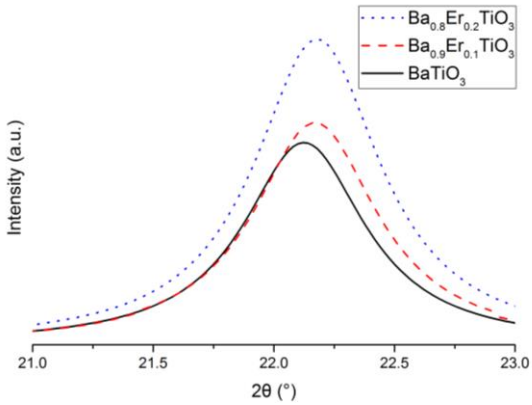

Fig. 2. Enlarged (001) (100) peaks for $Ba_{1-x}Er_xTiO_3$ thin films

XRD patterns can be utilized to estimate lattice parameters, such as interplanar spacing, *d*, lattice cell lengths, *a*, *c*, and unit cell volume, *V*. The spacing can be calculated from the Bragg equation given by:

$$\lambda = 2d \sin\theta \ , \tag{1}$$

while the lattice constants and unit cell volume can be evaluated using the lattice geometry equations as follow [12]:

$$\frac{1}{d^2} = \frac{h^2 + k^2}{a^2} + \frac{l^2}{c^2} \ ; \tag{2}$$

$$V = a^2 c \ . \tag{3}$$

The lattice parameters of the $Ba_{1-x}Er_xTiO_3$ thin films are listed in Table 1. The obtained lattice values indicate that the prepared $Ba_{1-x}Er_xTiO_3$ thin films exhibit tetragonal structure at room temperature. Furthermore, it is noticed that volume of $Ba_{1-x}Er_xTiO_3$ lattices is shrinking as *x* value increases, this is attributed to the smaller ionic radius of Er^{3+} (0.96 Å) compared to Ba^{2+} (1.35 Å).

3.2. Crystallite size and strain

A crystal would deviate from ideal crystallinity due to its restricted size, leading to a broadening in the diffraction lines. The broadening in XRD patterns is related to two main properties from peak width analysis, which are crystallite size and lattice strain [13]. Crystallite size is known as coherently diffracting domain size and it does not share the similar value with the particle size in a polycrystalline aggregates [14]. Lattice strain refers to the measurement of the distribution of the lattice constants that caused due to crystal imperfection [13]. In this paper, the geometric parameters have been evaluated using X-ray line profile analysis via different approaches, namely Scherrer equation, Williamson-Hall analysis, and size-strain plot method.

Table 1. Lattice parameters of $Ba_{1-x}Er_xTiO_3$ thin films

Sample	*a*, Å	*c*, Å	*V*, Å^3	*c*/*a*	Structure
$BaTiO_3$	4.0130	4.0423	65.0977	1.0073	Tetragonal
$Ba_{0.9}Er_{0.1}TiO_3$	3.9990	4.0434	64.6608	1.0111	Tetragonal
$Ba_{0.8}Er_{0.2}TiO_3$	3.9922	4.0490	64.5323	1.0142	Tetragonal

3.2.1. Scherrer equation

Crystallite size, D can be obtained from the Scherrer equation given by:

$$D = \frac{k\lambda}{\beta_D \cos\theta} \ , \tag{4}$$

where, k is Scherrer constant and it equals to 0.9, λ is the wavelength of $CuK_{\alpha 1}$ radiation, β is the peak width at half maximum intensity, and θ is the peak position.In practical scanning, instrument always contributes extra broadening to the peak width measured at Bragg angle [15]. Thus, it is necessary to eliminate the instrumental factor from the diffraction pattern using standard material, such as pure silicon. The instrumental corrected peak width, β_D due to the diffraction peak of the $Ba_{1-x}Er_xTiO_3$ thin films can be determined using the following equation:

$$\beta_D^2 = \beta_{\text{measured}}^2 + \beta_{\text{instrumental}}^2 . \tag{5}$$

The estimated average crystallite size values of the annealed $Ba_{1-x}Er_xTiO_3$ thin films are summarized in Table 2. From the table, one can observe that $Ba_{1-x}Er_xTiO_3$ thin films own nano crystalline structure. Furthermore, the crystallite size decreases as the Er doping concentration increases, which could be also due to the small ionic radius of Er^{3+} compared to Ba^{2+}.

Table 2. Crystallite size of $Ba_{1-x}Er_xTiO_3$ thin films

Sample	D, nm
$BaTiO_3$	13.18
$Ba_{0.9}Er_{0.1}TiO_3$	12.39
$Ba_{0.8}Er_{0.2}TiO_3$	12.16

3.2.2. Williamson-Hall analysis

Neglecting the broadening that caused by the lattice strain due to dislocation could lead to underestimating the crystallite size. The strain-induced broadening is firstly discovered by Stokes and Wilson, and the maximum strain given by [16, 17]:

$$\varepsilon = \frac{\beta_\varepsilon}{4 \tan\theta} . \tag{6}$$

Later on, Williamson and Hall combined the size-induced broadening, β_D, and strain-induced broadening, β_ε, in the following equation to separate the two main different factors for a line broadening [13]. However, the value of β_D and β_ε are dependent on the crystal nature.

$$\beta_{hkl} = \beta_D + \beta_\varepsilon \ . \tag{7}$$

According to the isotropic nature of the crystal, material properties are independent on the direction of the measurement. Hence, the strain is assumed to be uniform in all crystallographic directions. In this case, the size and strain induced broadening from Eq. 4 and Eq. 6, respectively, can be substituted into Eq. 7, leading to the following equation:

$$\beta_{hkl} = \frac{k\lambda}{D \cos\theta_{hkl}} + 4\varepsilon \tan\theta_{hkl} \ . \tag{8}$$

Rearranging Eq. 8 gives:

$$\beta_{hkl} \cos\theta_{hkl} = \frac{k\lambda}{D} + 4\varepsilon \sin\theta_{hkl} \ . \tag{9}$$

This equation is known as Williamson-Hall uniform deformation model (UDM). If $\beta_{hkl} \cos\theta_{hkl}$ in Eq. 9 is plotted as a function of 4 $\sin\theta_{hkl}$ as shown in Fig. 3 and the data is fitted linearly, the crystallite size can be extracted from the y-intercept, and the lattice strain can be estimated from the slope of the fitting line. The values of crystallite size and lattice strain obtained using UDM are inserted in Table 3.

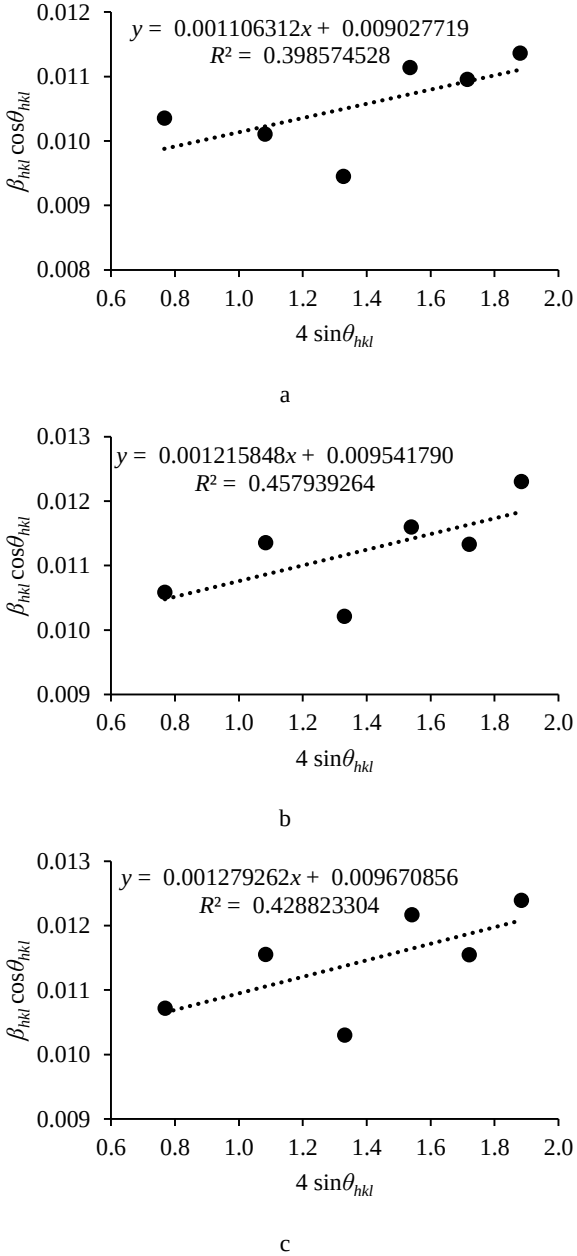

Fig. 3. Williamson-Hall UDM plots for: a – $BaTiO_3$; b – $Ba_{0.9}Er_{0.1}TiO_3$; c – $Ba_{0.8}Er_{0.2}TiO_3$ thin films

In realistic conditions, material properties are always vary with the crystallographic directions, thus, homogeneity and isotropic nature of crystal is hard to be achieved. A more physical approach for Williamson-Hall analysis can be accomplished by including the anisotropic magnitude, ε_{hkl} into the calculation. In uniform stress deformation model

(USDM), a lattice deformation stress, σ is applied to the crystal. The stress are assumed to be uniform in all directions. In this case, ε in Eq. 9 has to be replaced by an anisotropic strain, ε_{hkl}. According to the Hooke's law, for small deformation and the elongation of the crystal within the elastic limit, the ε_{hkl} gives the linear proportionality with the Young's modulus of the material in direction perpendicular to the set of the crystal lattice planes (*hkl*), E_{hkl}, or $\varepsilon_{hkl} = \sigma \,/\, E_{hkl}$. Considering these conditions, Eq. 9 can be reconstructed as follow:

$$\beta_{hkl}\cos\theta_{hkl} = \frac{k\lambda}{D} + \frac{4\sin\theta_{hkl}}{E_{hkl}} \cdot \sigma \,. \tag{10}$$

In USDM, if $4\sin\theta_{hkl} / E_{hkl}$ is plotted against $\beta_{hkl}\cos\theta_{hkl}$ and the data is fitted linearly as shown in Fig. 4, the crystallite size can be extracted from the y-intercept, and the stress of the material can be estimated from the gradient of the fitting line. The strain can be obtained from Young's Modulus, E_{hkl} due to the linear proportionality as discussed earlier. However, Zhang *et al.* reported that E_{hkl} for every crystalline material is related to its elastic compliances, s_{ij}, and crystal lattice plane (*hkl*), and for tetragonal crystal it is given as follow [18]:

$$\frac{1}{E_{hkl}} = \left[\frac{s_{11}\left(h^4 + k^4\right) + (2s_{12} + s_{66})h^2k^2}{\left[h^2 + k^2 + \left(\frac{al}{c}\right)^2\right]^2} + \frac{(2s_{13} + s_{44})(h^2 + k^2)\left(\frac{al}{c}\right)^2 + s_{33}\left(\frac{al}{c}\right)^4}{\left[h^2 + k^2 + \left(\frac{al}{c}\right)^2\right]^2}\right] \,. \tag{11}$$

The values of s_{11}, s_{12}, s_{13}, s_{33}, s_{44}, and s_{66} for $BaTiO_3$ ceramics are 8.05 x 10^{-12}, -2.35 x 10^{-12}, -5.24 x 10^{-12}, 15.7 x 10^{-12}, 18.4 x 10^{-12}, and 8.84 x 10^{-12} m^2 N^{-1}, respectively [19]. The values of the calculated Young's modulus via Eq. 11 for $BaTiO_3$, $Ba_{0.9}Er_{0.1}TiO_3$, and $Ba_{0.8}Er_{0.2}TiO_3$ are ~ 113, ~ 143, and ~ 143 GPa, respectively. The values of crystallite size, lattice strain, and stress obtained through USDM are listed in Table 3.

If the strain energy density, *u*, which is given according to Hooke's Law for elastic system by:

$$u = \frac{\varepsilon_{hkl}^2 E_{hkl}}{2} \tag{12}$$

is taken into account, the constants of proportionality associated with the stress-strain relation are no longer independent. In this case, Williamson-Hall, Eq. 9, can be modified to uniform deformation energy density model (UDEDM) as follow:

$$\beta_{hkl}\cos\theta_{hkl} = \frac{k\lambda}{D} + 4\sin\theta_{hkl}\sqrt{\frac{2}{E_{hkl}}} \cdot \sqrt{u} \quad . \tag{13}$$

If $\beta_{hkl}\cos\theta_{hkl}$ is plotted as a function of $4\sin\theta_{hkl}(2/E_{hkl})^{1/2}$ as shown in Fig. 5, the crystallite size and energy density are estimated from the y-intercept and the slope of the fitting line of the plot, respectively. The strain can be obtained using Eq. 12 while the stress can be acquired using the following equation:

$$\sigma = \sqrt{2uE_{hkl}} \quad . \tag{14}$$

The estimated values of crystallite size, lattice strain, stress, and energy density according to UDEDM can be found in Table 3.

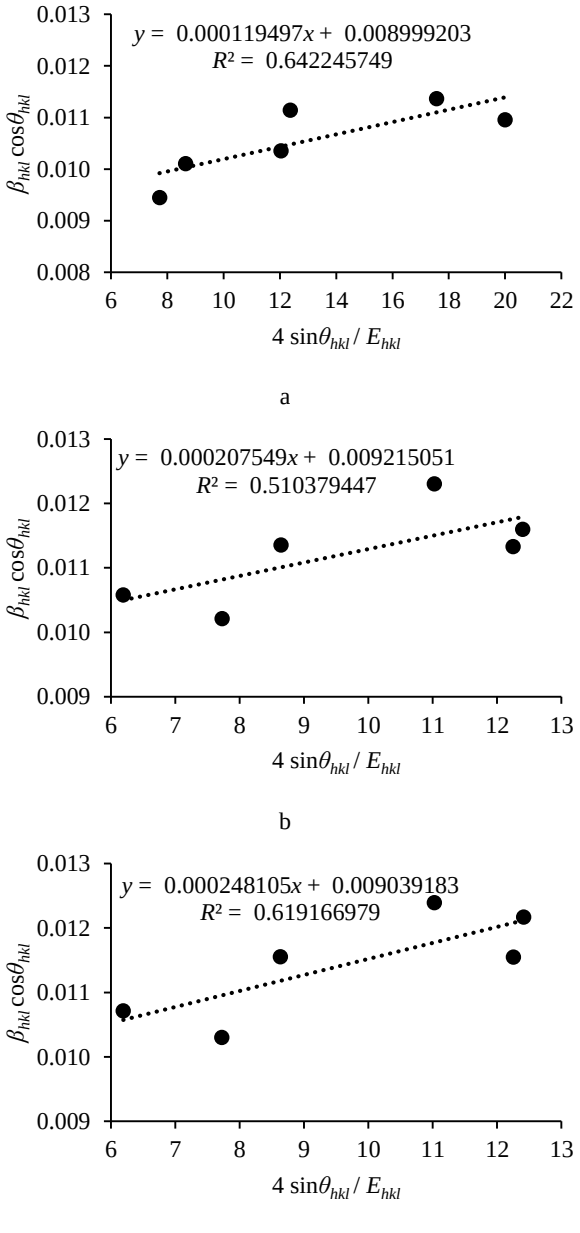

Fig. 4. Williamson-Hall USDM plots for: a – $BaTiO_3$; b – $Ba_{0.9}Er_{0.1}TiO_3$; c – $Ba_{0.8}Er_{0.2}TiO_3$ thin films

Table 3. Geometric parameters of $Ba_{1-x}Er_xTiO_3$ thin films using Williamson-Hall analysis

Sample	UDM			UDSM				UDEDM				
	D, nm	ε (x10^{-3})	R^2	*D*, nm	ε (x10^{-3})	σ, MPa	R^2	*D*, nm	ε (x10^{-3})	σ, MPa	*u*, kJ/m^3	R^2
$BaTiO_3$	15.36	1.106	0.399	15.41	1.058	120	0.642	15.90	1.302	147	96	0.643
$Ba_{0.9}Er_{0.1}TiO_3$	14.53	1.216	0.458	15.05	1.453	208	0.510	14.99	1.430	204	146	0.519
$Ba_{0.8}Er_{0.2}TiO_3$	14.34	1.279	0.429	15.34	1.736	248	0.619	15.03	1.605	229	184	0.554

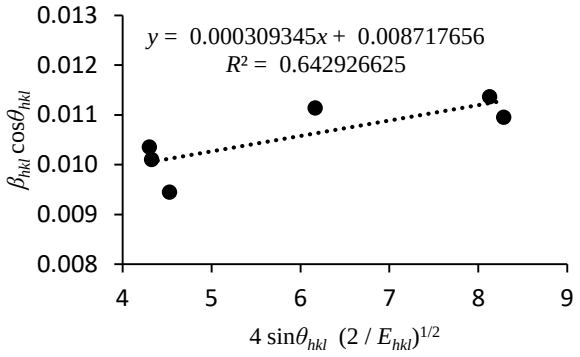

a

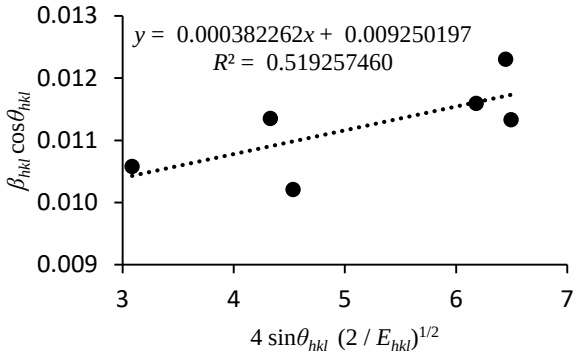

b

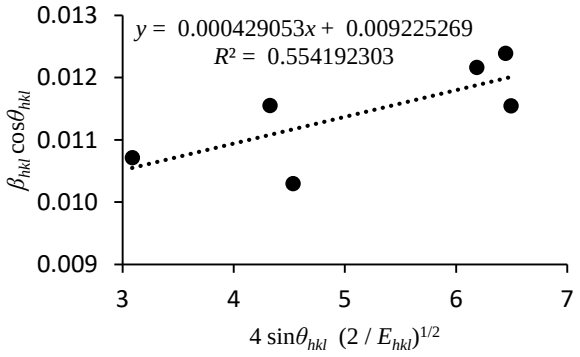

c

Fig. 5. Williamson-Hall UDEDM plots for: a – $BaTiO_3$; b – $Ba_{0.9}Er_{0.1}TiO_3$; c – $Ba_{0.8}Er_{0.2}TiO_3$ thin films

It can be seen from Table 3 that the crystallite size of the tested films using Williamson-Hall analysis has larger values compared to the one estimated via Scherrer equation, which is attributed to the contribution of the lattice strain. It is also noticed that the microstrain increases as $BaTiO_3$ is doped with Er^{3+} ions. The microstrain could be created due to the lattice distortion as a result of substitution of small ionic radius Er^{3+} ions into Ba^{2+} sites in the perovskite lattice. Furthermore, as the doping concentration increases, the lattices gain more distortion that reflected as broader peak in XRD to be obtained. As a result, smaller crystallite size is grown.

It is observed that after considering the anisotropic nature of $Ba_{1-x}Er_xTiO_3$ thin films, the crystallite size value does not show noticeable change compared to the isotropic UDM model.

It is noticed that the data points for all plots are scattered away from the fitting lines, which due to considering the parameters that causes the broadening in peaks into account. In order to evaluate the best fitting among the Williamson-Hall models for the current films, the goodness of fit R^2 is used and its values usually varies from 0 to 1. Generally, R^2 value of 1 indicates a perfect fitting, while R^2 value less than 1 shows that at least some variability are unable to be accounted by the fitting [20]. It is noticed that the fitting for samples according to UDEDM possesses high R^2 values compared to other models. This suggests that the UDEDM could have the best fitting among other Williamson-Hall models for this kind of material.

3.2.3. Size-strain plot (SSP)

X-ray line profile analysis using Williamson-Hall method for isotropic line broadening denotes that the isotropic nature of diffracting domains and the presence of microstrain involvement. However, the average "size-strain plot" (SSP) offers a better valuation of size-strain parameters in case of isotropic line broadening [21]. This method suggests the advantage that less emphasis is assigned to the data from high angle reflections, where the precision is typically poorer. In this approximation, Lorentzian function is assumed to fit the "crystallite size" profile while Gaussian function is applied to the "strain" profile [21]. Such hypothesis gives the relationship stated as below:

$$\left(d_{hkl}\ \beta_{hkl}\cos\theta_{hkl}\right)^2 = \frac{1}{V_S}\ d_{hkl}^2\,\beta_{hkl}\cos\theta_{hkl} + \left(\frac{\varepsilon_a}{2}\right)^2, \qquad (15)$$

where d_{hkl} is the lattice distance between the (hkl) plane, V_S is the apparent weighted average size, ε_a is apparent strain which is related to the root-mean-square (rms) strain, ε_{rms} according to the following equation:

$$\varepsilon_{\text{rms}} = \frac{\varepsilon_a}{2\sqrt{2\pi}}. \qquad (16)$$

In the case of a spherical crystallites, the volume average true crystallite size is given as follow:

$$D_V = \frac{4}{3}\ V_S. \qquad (17)$$

Using Eq. 15, $(d_{hkl}\,\beta_{hkl}\cos\theta_{hkl})^2$ is plotted against $d_{hkl}^2\,\beta_{hkl}\cos\theta_{hkl}$ for $Ba_{1-x}Er_xTiO_3$ perovskite peaks as shown in Fig. 6. Accordingly, with the aid of Eq. 16 and Eq. 17, the rms strain, ε_{rms}, and the volume average true crystallite size, D_V are evaluated from the y-intercept and the slope of the linear fitting line, respectively. The crystallite size and lattice strain of the $Ba_{1-x}Er_xTiO_3$ thin films found using this method are listed in Table 4.

Table 4. Geometric parameters of $Ba_{1-x}Er_xTiO_3$ thin films using SSP

Sample	D, nm	ε (x10^{-3})	R^2
$BaTiO_3$	13.08	1.524	0.997
$Ba_{0.9}Er_{0.1}TiO_3$	12.83	2.649	0.996
$Ba_{0.8}Er_{0.2}TiO_3$	12.70	2.863	0.995

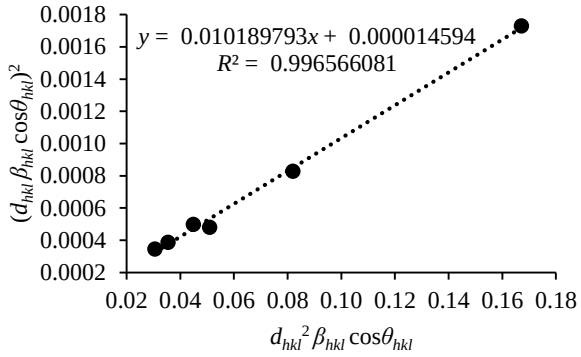

a

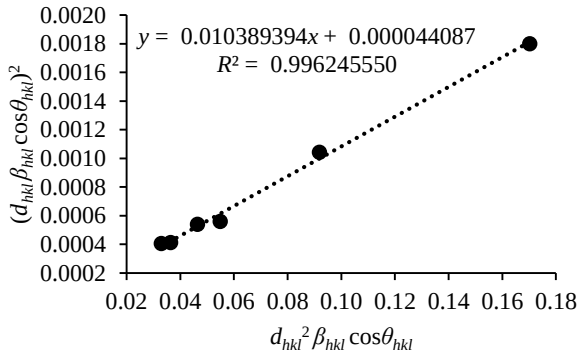

b

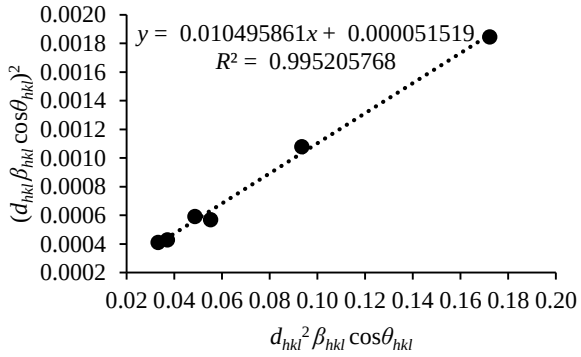

c

Fig. 6. Size-strain plots for: a – $BaTiO_3$; b – $Ba_{0.9}Er_{0.1}TiO_3$; c – $Ba_{0.8}Er_{0.2}TiO_3$ thin films

It can be noticed that the fitting via SSP method possesses higher goodness of fit values compared to the Williamson-Hall methods that discussed in section 3.2.2, where the center of all data points in SSP technique lay exactly on the fitting line, but in Williamson-Hall methods, the data points scattered around the fitting line, which lead us to conclude that SSP method could be the better approach to obtain crystallite size and lattice strain for this kind of material.

4. CONCLUSIONS

In this work, sol-gel perovskite $Ba_{1-x}Er_xTiO_3$ thin films have been successfully fabricated on SiO_2/Si substrate. The crystalline structure for the films has been investigated using XRD, which shows that $Ba_{1-x}Er_xTiO_3$ thin films are crystallized with tetragonal structure at room temperature. The increment in x value shows broadening and shifting for perovskite peaks towards higher angle. The effect of Er^{3+} ions substituted into Ba^{2+} sites within the $BaTiO_3$ lattices is investigated using Scherrer, Williamson-Hall, and SSP methods. It is found that the estimated crystallite size of the films using all approaches decreases as Er^{3+} ions concentration increases. In addition, Williamson-Hall and SSP methods reveal that the microstrain, created due to the distortion in the perovskite lattice as a result of substitution of relatively small ionic radius for Er^{3+} ions compared to Ba^{2+} ions, increases as Er^{3+} ions concentration increases that is visualized as broader peak, which in turn reduces the crystallite size. Among the line profile analysis methods, SSP shows the best fitted graphs with goodness of fit R^2 close to 1, leading to high accuracy of the obtained values, which suggests that SSP could be a better choice to analyze crystallite size and lattice strain for this sort of material.

Acknowledgments

This work is supported by the Fundamental Research Grant Scheme (FRGS) with the Grant number 9003-00479, funded by the Ministry of Higher Education (KPT).

REFERENCES

1. **Chen, L., Wei, X.H., Fu, X.** Effect of Er Substituting Sites on Upconversion Luminescence of Er^{3+}-doped $BaTiO_3$ Films *Transactions of Nonferrous Metals Society of China* 22 (5) 2012: pp. 1156 – 1160. https://dx.doi.org/10.1016/S1003-6326(11)61299-5
2. **Maneeshya, L.V., Thomas, P.V., Joy, K.** Effects of Site Substitutions and Concentration on the Structural, Optical and Visible Photoluminescence Properties of Er doped $BaTiO_3$ Thin Films Prepared by RF Magnetron Sputtering *Optical Materials* 46 2015: pp. 304 – 309. https://dx.doi.org/10.1016/j.optmat.2015.04.036
3. **Gill, D.M., Ford, G.M., Block, B.A., Wessels, B.W., Ho, S. T.** Guided Wave Fluorescence in Thin Film Er-doped Barium Titanate *Materials Research Society Proceedings* 486 1997: pp. 343. https://dx.doi.org/10.1557/PROC-486-343
4. **Rehani, B.R., Joshi, P.B., Lad, K.N., Pratap, A.** Crystallite Size Estimation of Elemental and Composite Silver Nano-powders using XRD Principles *Indian Journal of Pure and Applied Physics* 44 (2) 2006: pp. 157 – 161. http://nopr.niscair.res.in/handle/123456789/8253
5. **Chidambara Kumar, K.N., Khadeer Basha, S.K., Shakil Muhammad, G.** X Ray Line Profile Analysis of Mn doped PbS Thin Films by Successive Ionic Layer Adsorption and Reaction Method *International Journal of ChemTech Research* 7 (5) 2015: pp. 2257 – 2264. http://sphinxsai.com/2015/ch_vol7_no5/ch03.htm
6. **Siddaramanna, A., Srivastava, C., Narayana Rao, B., Ranjan, R.** Effect of Crystallite Size and Clustering in Influencing the Stability of Phases of A Very Large Tetragonality Ferroelectric System $0.6BiFeO_3$–$0.4PbTiO_3$ *Solid State Communications* 160 2013: pp. 56 – 60. http://dx.doi.org/10.1016/j.ssc.2013.02.014
7. **Thool, G. S., Singh, A.K., Singh, R.S., Gupta, A., Hasan Susan, M.A.B.** Facile Synthesis of Flat Crystal ZnO Thin Films by Solution Growth Method: A Micro-structural Investigation *Journal of Saudi Chemical Society* 18 (5) 2014: pp. 712 – 721. http://dx.doi.org/10.1016/j.jscs.2014.02.005
8. **Mahmood, N.B., Al-Shakarchi, E.K.** Three Techniques

Used to Produce $BaTiO_3$ Fine Powder *Journal of Modern Physics* 2 (11) 2011: pp. 1420 – 1428. https://dx.doi.org/10.4236/jmp.2011.211175

9. **Chrunik, M.J., Kłosowicz, S., Perkowski, P., Mrukiewicz, M., Morawiak, P., Zasada, D.** The Influence of Microstructure and Lattice Strain on Tetragonality Factor and Dielectric Properties of Ferroelectric Ceramics $BaTiO_3$ *Acta Physica Polonica A* 124 (6A) 2013: pp. 1034 – 1038. https://dx.doi.org/10.12693/APhysPolA.124.1034
10. **Mahata, M.K., Kumar, K., Rai, V.K.** Structural and Optical Properties of Er^{3+}/Yb^{3+} doped Barium Titanate Phosphor Prepared by Co-precipitation Method *Spectrochimica Acta Part A: Molecular and Biomolecular Spectroscopy* 124 2014: pp. 285 – 291. http://dx.doi.org/10.1016/j.saa.2014.01.014
11. **Zaumseil, P.** High-resolution Characterization of the Forbidden Si 200 and Si 222 Reflections *Journal of Applied Crystallography* 48 (2) 2015: pp. 528 – 532. http://dx.doi.org/10.1107/S1600576715004732
12. **Cullity, B.D.** Elements of X-ray Diffraction. Addison-Wesley Pub. Co., Reading, 2001.
13. **Yogamalar, R., Srinivasan, R., Vinu, A., Ariga, K., Bose, A.C.** X-ray Peak Broadening Analysis in ZnO Nanoparticles *Solid State Communications* 149 (43 – 44) 2009: pp. 1919 – 1923. http://dx.doi.org/10.1016/j.ssc.2009.07.043
14. **Ramakanth Hebbar, K.** Basics of X-ray Diffraction and Its Applications. I.K. International Pub. House, New Delhi, 2007.
15. **Rogers, K.D., Daniels, P.** An X-ray Diffraction Study of the Effects of Heat Treatment on Bone Mineral Microstructure *Biomaterials* 23 (12) 2002: pp. 2577 – 2585. http://dx.doi.org/10.1016/S0142-9612(01)00395-7
16. **Stokes, A.R., Wilson, A.J.C.** A Method of Calculating the Integral Breadths of Debye-Scherrer Lines: Generalization to Non-cubic Crystals *Mathematical Proceedings of the Cambridge Philosophical Society* 40 (2) 1944: pp. 197 – 198. http://dx.doi.org/10.1017/S0305004100018314
17. **Mittemeijer, E.J., Welzel, U.** The "State of the Art" of the Diffraction Analysis of Crystallite Size and Lattice Strain *Zeitschrift für Kristallographie – Crystalline Materials* 223 (9) 2008: pp. 552 – 560. https://dx.doi.org/10.1524/zkri.2008.1213
18. **Zhang, J.M., Zhang, Y., Xu, K.W., Ji, V.** Young's Modulus Surface and Poisson's Ratio Curve for Tetragonal Crystals *Chinese Physics B* 17 (5) 2008: pp. 1565 – 1573. http://dx.doi.org/10.1088/1674-1056/17/5/006
19. **Gray, D.E.,** American Institute of Physics Handbook. McGraw-Hill, New York, 1972: pp. 2 – 54.
20. **Hamilton, D.F., Ghert, M., Simpson, A.H.R.W.,** Interpreting Regression Models in Clinical Outcome Studies *Bone and Joint Research* 4 (9) 2015: pp. 152 – 153. http://dx.doi.org/10.1302/2046-3758.49.2000571
21. **Tagliente, M.A., Massaro, M.** Strain-driven (002) Preferred Orientation of ZnO Nanoparticles in Ion-implanted Silica *Nuclear Instruments and Methods in Physics Research Section B: Beam Interactions with Materials and Atoms* 266 (7) 2008: pp. 1055 – 1061. http://dx.doi.org/10.1016/j.nimb.2008.02.036